A FRET-based Sensor of Steric Pressure on Membrane Surfaces

Authors

Justin R. Houser[1], Carl C. Hayden[1], D. Thirumalai[2], Jeanne C. Stachowiak[1,3]*

Affiliations

[1]Department of Biomedical Engineering, The University of Texas at Austin

[2]Department of Chemistry, The University of Texas at Austin.

USA

[3]Institute for Cellular and Molecular Biology, The University of Texas at Austin,

**To whom correspondence should be addressed: jcstach@austin.utexas.edu*

Abstract

Cellular membranes are densely covered by proteins. Steric pressure generated by protein collisions plays a significant role in shaping and curving biological membranes. However, no method currently exists for measuring steric pressure at membrane surfaces. Here we develop a sensor based on Förster resonance energy transfer (FRET), which uses the principles of polymer physics to precisely detect changes in steric pressure. The sensor consists of a polyethylene glycol chain tethered to the membrane surface. The polymer has a donor fluorophore at its free end, such that FRET with acceptor fluorophores in the membrane provides a real-time readout of polymer extension. As a demonstration of the sensor, we measured the steric pressure generated by a model protein involved in membrane bending, the ENTH domain of Epsin1. As the membrane becomes crowded by ENTH proteins, the polymer chain extends, increasing the fluorescence lifetime of the donor. Drawing on polymer theory, we use this change in lifetime to calculate steric pressure as a function of membrane coverage by ENTH, validating theoretical equations of state. Further, we find that ENTH's ability to breakup larger vesicles into smaller ones correlates with steric pressure rather than the chemistry used to attach ENTH to the membrane surface. This result addresses a long-standing question about the molecular mechanisms of membrane remodeling. More broadly, this sensor makes it possible to measure steric pressure in situ during diverse biochemical events that occur on membrane surfaces, such as membrane remodeling, ligand-receptor binding, assembly of protein complexes, and changes in membrane organization.

Introduction

The assembly of curved membrane structures plays a fundamental role in cell physiology from membrane traffic to cell motility and cytokinesis [1]. Two broad physical mechanisms have been proposed to explain how proteins shape membranes. First proteins with inherently curved domains, such as crescent-shaped BAR (bin/amphiphysin/rvs) domains and clathrin triskelia, are thought to scaffold the membrane surface [2-3]. Second, proteins such as Epsin1 and AP180 are thought to insert wedge-like amphipathic helices into the membrane surface, driving curvature [4].

While the scaffolding and insertion mechanisms each rely on specific protein structural features, recent work has shown that non-specific effects, such as steric interactions among proteins, can also generate the pressure required to bend membranes [5]. In some cases, this steric pressure, rather than specific structural motifs, appears to be the primary driver of membrane remodeling. For example, our recent work has shown that membrane bending by the N-terminal homology domain (ENTH) of the endocytic protein, Epsin1, does not depend on insertion of an amphipathic helix into the membrane, as had been previously accepted [4, 6]. Instead, we found that bending occurs when a critical concentration of ENTH domains bind to the membrane surface, regardless of whether they attach by inserting an amphipathic helix or using an engineered tag. These findings, in parallel with recent work by the Baumgart lab [7-8], suggest that pressure created by collisions between membrane-bound proteins drives bending. Similarly, a recent report has shown that steric pressure among glycosylated proteins on the extracellular face of the plasma membrane can drive the formation of outward membrane protrusions that resemble filopodia [9]. Additionally, intrinsically disordered proteins, which, for a given molecular weight, have larger hydrodynamic radii than folded proteins, have been shown in several recent studies to drive dramatic membrane remodeling events, when they exceed threshold densities on membrane surfaces [3, 10-11].

Collectively these studies suggest that steric pressure at membrane surfaces provides a potent driving force for membrane remodeling. However, a key challenge has been to determine the magnitude of this pressure and measure it in the context of membrane remodeling events. Presently, no measurements exist of steric pressure among proteins within the two-dimensional plane of a biological membrane. Instead, measurements of protein density on membrane surfaces have been combined with results from crowded particle theory to estimate the magnitude of steric pressure [6, 12]. Importantly, the accuracy of these expressions has yet to be experimentally evaluated, making it difficult to precisely account for the impact of steric pressure in models of membrane remodeling and organization.

Toward filling this gap, here we develop a polymer-based sensor of steric pressure at membrane surfaces, which is based on Förster resonance energy transfer (FRET). We measure FRET between a donor fluorophore at the free end of a membrane-bound polymer, and acceptor fluorophores embedded in the membrane surface. This approach was inspired by the recent use of polymer-based sensors to measure steric pressure in crowded solutions [13]. When the concentration of membrane-bound proteins and the resulting steric pressure was low, the polymer probe had a short end-to-end distance, as indicated by a shift in the donor fluorescence decay toward shorter times. In contrast, as protein concentration and steric pressure increased, the polymer became extended, corresponding to a substantial shift in the donor fluorescence decay towards longer times. Using the theory of tethered polymers [14-15], the donor fluorescence decay was modeled to determine the change in polymer conformational entropy and steric pressure in the plane of the membrane surface. The resulting relationship between steric pressure and membrane coverage by the ENTH domain was in good agreement with the predictions of crowded particle theory, validating previous estimates [11, 16]. As the coverage of the membrane surface by ENTH domains increased, the vesicles began to undergo membrane fission, breaking up into smaller vesicles. Interestingly, the resulting relationship between vesicle diameter and membrane coverage remained the same, whether ENTH bound to the membrane surface using its amphipathic helix or an engineered tag. This result suggests that protein crowding, rather than amphipathic helix insertion, is the primary driver of steric pressure and membrane remodeling by the ENTH domain. As illustrated by these results, our sensor enables, for the first time, a direct measure of the steric pressure needed to induce membrane fission. More broadly, the sensor developed here, which is based on fundamental concepts in polymer physics, can be applied to assess the ability of a wide variety of membrane-bound proteins to generate steric pressure, driving changes in membrane shape, while also controlling the organization [17], and mobility [18] of lipids and proteins at membrane surfaces.

Results and Discussion

Design and calibration of a membrane-bound, FRET-based sensor

The sensor used in this work consisted of an amine-terminated, polyethylene glycol (PEG) chain that was covalently attached by the manufacturer to the headgroup of a synthetic phospholipid, 1,2-distearoyl-*sn*-glycero-3-phosphoethanolamine (DSPE). These lipids were incorporated into membrane vesicles at 1 mol%. The amine group at the free end of the polymer was labeled with NHS-ester Atto 488, a green fluorescent dye. This dye molecule, which has been shown to have minimal non-specific interactions with membrane surfaces [19], served as the FRET donor fluorophore. The FRET acceptor fluorophores resided within the membrane surface, which contained 2.5-10 mol% Texas Red DHPE (1,2-dihexadecanoyl-*sn*-glycero-3-phosphoethanolamine, triethylammonium salt). The remainder of the lipids within the vesicles consisted of 89-96.5 mol% 1,2-dioleoyl-*sn*-glycero-3-phosphocholine (DOPC). The vesicles were formed using standard procedures described in the methods section, and were extruded through a filter with a mean pore diameter of 100 nm, resulting in vesicles with an average diameter of 109 to 115 nm, as determined using dynamic light scattering.

The FRET sensor and its incorporation into lipid vesicles is depicted in Figure 1A. Because the conjugation of the Atto 488 dye was performed after extrusion of the vesicles, only PEG chains displayed on the outer surfaces of the membrane vesicles were labeled. As the density of acceptor fluorophores in the membrane increased from 2.5 mol% to 10 mol%, the donor fluorescence decay shifted substantially toward shorter times, Figure 1B. In all further studies, 10 mol% of the acceptor fluorophore was used, in order to maximize the FRET effect. For these measurements, the length of the PEG chain was held constant at 5 kDa. Next we varied the length of the PEG chain and measured the impact on the donor fluorescence decay. As depicted in Figure 1A, the separation between the donor and acceptor fluorophores should increase as the length of the PEG chain increases. As expected, the donor fluorescence decay shifted toward longer times, as the length of the PEG chain increased, Figure 1C. Notably, a high degree of precision was achieved in the fluorescence lifetime data owing to the use of relatively long, 150-200 s, dwell times, during which many different lipid vesicles diffuse through the laser focal volume. As a result, the photon counted histograms in Figures 1 integrate information from many different probe molecules across a large population of lipid vesicles.

We next sought to relate the donor fluorescence decay, which is a distribution of donor lifetimes, to the distribution of polymer end to end distances. DiMarzio and McCrakin have derived an analytical relationship that describes the distribution of end to end distances for a one-dimensional, freely-jointed polymer chain, which is tethered to a surface [14-15], equation 1.

$$P_{chain}(N,z) = \left(\frac{2}{\pi N}\right)^{\frac{1}{2}} \left(\frac{2^{N+1}(z+1)}{N}\right) \exp\left(-\frac{z^2}{2N}\right) \quad (1)$$

For a polymer of N rigid segments, $P_{chain}(N,z)$ is the probability of a particular end to end distance, z, in units of rigid segment number. For a freely-jointed chain, the length of each rigid segment, or Kuhn length, is equivalent to the persistence length [20], a quantity which is often measured in experiments. When comparing this model to a real, three-dimensional polymer, N represents the number of rigid segments in the dimension normal to the membrane surface, which is approximately one third of the total number of segments in the polymer. We used this distribution, along with the relationship between fluorescence lifetime and donor-acceptor separation distance, to create a family of predicted donor fluorescence decay curves for polymer chains with an increasing number of segments, N. Specifically, for each value of z, holding N fixed, the probability of donor excitation P_{donor}, as a function of time, t, can be calculated using equation 2.

$$P_{donor}(t,z) = exp\left(-\frac{t}{\tau_{DA}}\right) \quad (2)$$

Here τ_{DA} is the donor lifetime in the presence of acceptors, at a distance, z. Given the high concentration of acceptor-labeled lipids in the membrane, we assume that there will always be an acceptor almost directly below the donor on the membrane surface, such that the acceptor and donor are only separated by the displacement of the donor along the axis perpendicular to the membrane surface. Notably, acceptor dyes were also present in the internal membrane leaflet, but were separated from the donor by the thickness of the membrane, an additional 3-5 nm. Owing to the extremely strong dependence of FRET on distance, this population of acceptors was expected to have a negligible impact on the lifetime of the donor and was therefore omitted from our calculations. Equation 3 describes FRET between the donor and acceptor, where τ_D is the donor lifetime in the absence of acceptors, R_0 is the Förster radius of the donor-acceptor dye pair, and r is the length of each rigid segment within the polymer.

$$\tau_{DA} = \frac{\tau_D}{1+\left(\frac{R_0}{zr}\right)^6} \quad (3)$$

This expression can be used to represent τ_{DA} in terms of z, r,R_0, and τ_D, resulting in equation 4.

$$P_{donor}(t,z) = exp\left(-\left(\frac{t}{\tau_D}\right)\left(1+\left(\frac{zr}{R_0}\right)^6\right)\right) \quad (4)$$

Once the donor fluorescence decays, $P_{donor}(t, z)$, have been calculated for all possible values of z, and fixed N, the expected fluorescence decay from the tethered polymer, P_{decay}, can be expressed as the sum of these decays, each weighted by its normalized probability within the distribution in equation 1, P_{chain}^{normal}, yielding equation 5.

$$P_{decay}(t, N) = \sum_{z=0}^{z=N} \left(P_{donor}(t)\right) \left(P_{chain}^{normal}(N, z)\right) \qquad (5)$$

P_{decay} was calculated for a range of possible N values, and convoluted with the instrument response function as determined from the measured instrument response to signal from nonresonant Raman scattering in water. Then, with N as the only free parameter, we chose the calculated distribution with the least sum of squared error relative to the experimentally measured distributions in Figure 1C. Here the rigid segment length, r, which is equivalent to the persistence length for a freely-jointed chain [20], was held fixed at the experimentally measured value [21] of 3.8 angstroms. The value of R_0 was chosen such that the data for all chain lengths were best fit by calculated decay curves corresponding closely to the known number of segments, N, within the polymer chains. The resulting value of R_0, 50 angstroms, is similar to the value of R_0 calculated form the fluorescence spectra of the donor and acceptor dyes, 54 angstroms.

An example comparing the experimentally measured decay curve for the PEG10K chain, along with the best fitting calculated decay curve, from equation 5, is shown in Figure 1D. Each of the other best fit comparisons are shown in Supporting Figure S1. In Figure 1E, the known number of rigid segments in the z-dimension for each of the polymer chains (2, 3.4, 5, 10 kDa) is compared with the predicted number of rigid segments in the best fit decay curves, where all fits were constrained to using the same value of R_0, 50 angstroms. The agreement is very good, demonstrating that the donor decay curve can be used to make reasonable predictions of the distribution of polymer conformations.

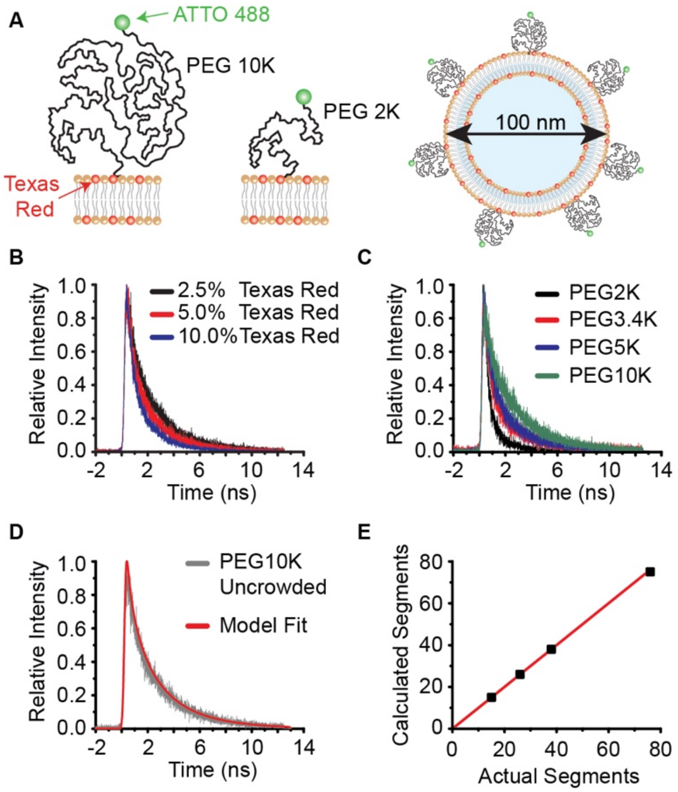

Figure 1 – Quenching of membrane-tethered donor fluorophores depends on polymer length and the density of acceptor fluorophores within the membrane. Vesicle composition is 89-96.5 mol% DOPC, 1 mol% PEG DSPE NH2 (varied PEG molecular weight), and 2.5-10 mol% Texas Red-DHPE extruded to 100 nm diameter. The FRET donor was ATTO 488 labeled PEG DSPE, with the label on the free end of the polymer. The FRET acceptor was Texas Red-DHPE. (A) Schematic of the FRET sensor. PEG chains of varying molecular weight were grafted to the surfaces of lipid vesicles consisting primarily of Texas Red-DHPE and DOPC. (B) Increasing the mol% of Texas Red-DHPE results in a shift toward shorter times in the decay curve of the ATTO 488 donor, tethered to the membrane is 5K PEG chains. 10 mol% Texas Red-DHPE was chosen for all further experiments for optimal FRET efficiency in our system. (C) Increasing the molecular weight of the PEG polymer on the surface of the lipid vesicles results in an overall increase in the separation between the acceptor and the donor, increasing the average donor lifetime. (D) Fit of a distribution of end-to-end lengths developed from polymer theory to our FRET decay curve for PEG 10K. (E) Comparison of the number of segments per PEG chain to the number of segments predicted by the best fit of the model. Here the red line has a slope of one. Curves in B are representative curves picked from 9-15 total trials. Curves in C-D are representative curves picked from two independent experiments, each consisting of 9-15 trials, for a total of 18-30 trials. Markers in E represent the average number of segments calculated for the data in C. Error bars in E were calculated as standard deviation of the mean (not visible due to being inside the width of the marker).

Crowding by proteins decreases the conformational entropy of the polymer probe.

Next we evaluated the impact of steric pressure on the donor fluorescence decay curve. In these studies the vesicles contained 5 mol% of the lipid phosphatidylinositol 4,5-bisphosphate (PI(4,5)P2) and 15 mol% 1,2-dioleoyl-*sn*-glycero-3-phospho-L-serine sodium salt (DOPS), both of which promote binding of the wild-type ENTH domain of Epsin 1, wtENTH, to the surfaces of the vesicles. As the concentration of wtENTH in solution increased from 500nM to 100 μM, the donor fluorescence decay shifted steadily toward longer times, Figure 2A. This shift suggests that the presence of the membrane-bound proteins drove an increase in the distribution of end-to-end distances of the membrane-bound polymer chains. This increase suggests that the membrane-bound proteins generate steric pressure that limits the conformational freedom of the polymer chains [22].

A decrease in the conformational freedom of a polymer chain can be modeled as a reduction in the number of freely-jointed segments within the chain. Specifically, as the concentration of membrane bound proteins increases, the steric repulsion between the proteins and the polymer chains should increase. Consequently, the conformational freedom of the polymer chains decreases. This decrease occurs because the chains are being confined by the neighboring proteins, where the degree of confinement increases as the coverage of the surface by proteins increases. This confinement stretches the chains, increasing their end-to-end distance. The resulting stretched conformations can be modeled by increasing the rigid segment length from r to r', which is equivalent to decreasing the number of segments in the chain, while maintaining a constant total chain length. The effective number of segments in the crowded chain is then given by equation 6, where N' is always less than N, the number of segments in the uncrowded polymer.

$$N' = N(r/r') \qquad (6)$$

In this way, a polymer chain that is experiencing a reduction in conformational freedom owing to steric pressure can be approximated as a chain of higher rigidity. Using this approach, we generated a new set of predicted donor fluorescence decay curves with a decreasing number of total segments, while holding the total chain length constant. We fit each of the measured donor fluorescence decay curves with this family of predicted curves in order to determine the effective number of segments per polymer chain associated with each concentration of membrane-bound proteins, as shown in Figure 2B,C. The sum of square error between the model decay and the data was calculated and the optimum segment length that minimized the error was determined. Using this approach we achieved excellent fits between the model calculation and the data for all crowding conditions, Figure 2B, Supporting Figure S2.

The reduction in the effective number of segments per chain can be used to estimate the associated reduction in chain entropy, S. Specifically, DiMarzio and McCrakin derived an analytical relationship between the number of polymer configurations, W, and the number of rigid segments, N, equation 7 [15].

$$W = \frac{2^N}{N^{1/2}} \qquad (7)$$

Using, Boltzmann's law, the change in free energy per chain associated with a change in segment number from N to N', can be approximated as follows, equation 8.

$$\Delta G = G' - G = T(S - S') = k_B T ln\left(\frac{W}{W'}\right) = k_B T\left((N - N')ln2 + \frac{1}{2}ln\left(\frac{N'}{N}\right)\right) \tag{8}$$

Using this approximation, Figure 2D plots the change in polymer free energy per polymer chain associated with steric pressure from the wtENTH proteins, as a function of the concentration of the wtENTH proteins in solution.

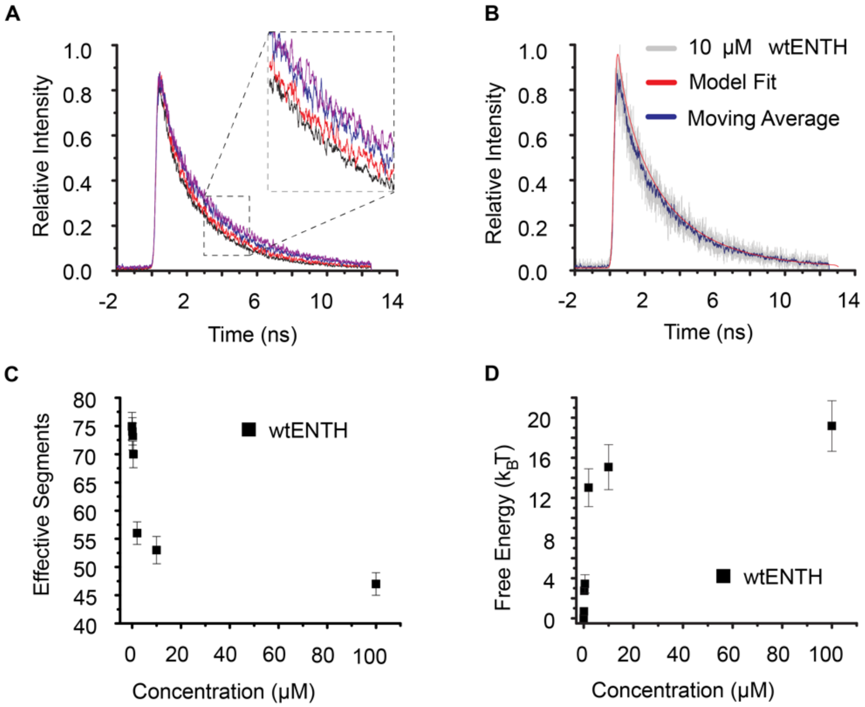

Figure 2 – FRET-based estimate of free energy generated by protein crowding. The membrane composition was 67 mol% DOPC, 15 mol % DOPS, 5 mol% PtdIns(4,5)P2, 2 mol% DP-EG10-biotin, 1 mol% PEG 10K-DSPE, and 10 mol% Texas Red-DHPE. Vesicles were extruded to a diameter of 100 nm. The FRET donor was ATTO 488 labeled PEG DSPE, with the label on the free end of the polymer. The FRET acceptor was Texas Red-DHPE. (A) Donor fluorescence decay curves upon crowding with increasing concentrations of wtENTH (uncrowded black line, 500nM red line, 10μM blue line, and 100μM purple line). Curves are displayed with a moving averages over a 10-point interval to better visualize the shift in decay curves. (B) Example of the model fit to the donor fluorescence decay curve in the presence of 10μM wtENTH. (C) Decrease in number of polymer segments needed to fit each donor fluorescence decay curve, as the concentration of wtENTH increased. (D) Calculated change in free energy from the data presented in C. Representative FRET curves for A and B were chosen from two independent experiments with 10-16 trials per experiment for a total of 20-32 trials. Markers in C-D represent an average from two to three independent experiments with 9-16 trials per experiment for a total of 18 to 48 total trials. Vertical axis error bars in C and D were calculated as the standard deviation of the mean.

The polymer probe reports changes in steric pressure with increasing protein crowding.

Steric pressure is expected to increase as proteins cover an increasing fraction of the membrane surface. Therefore, we sought to estimate the coverage of the membrane surface for vesicles exposed to each concentration of protein in solution. The coverage is the sum of the fraction of the membrane covered by polymer sensors, and the fraction covered by wtENTH proteins. The polymer sensor covered approximately 21% of the membrane surface based on the measured fraction of PEG-chains on the outer vesicle surfaces, and the projected area of each polymer chain on the membrane surface, 34 nm^2, Supporting Figure 3. This level of coverage is within the range of the density of membrane-bound proteins on the surfaces of biological membranes [23]. We used a quantitative fluorescence approach to estimate the average number of membrane bound proteins per lipid vesicle, as protein concentration in solution increased, an approach which we have previously validated [11], see methods. Briefly, vesicles containing 2 mol% of biotin-conjugated lipids were formulated (total composition: 76 mol% DOPC, 15 mol % DOPS, 5 mol% PtdIns(4,5)P2, 2 mol% DP-EG10-biotin, 1 mol% PEG 10K-DSPE, and 1 mol% Texas Red-DHPE). These vesicles were incubated with Alexa 647 labeled wtENTH in microcentrifuge tubes for 1 hour, which was long enough to allow protein binding to reach equilibrium. Following incubation, the vesicles were tethered to the surfaces of glass coverslips coated by biotin-conjugated PEG chains that had been exposed to neutravidin, Figure 3A. Once the vesicles were tethered, images of the tethered vesicles were acquired in both the labeled lipid (Texas Red) and protein (Alexa 647) fluorescent channels using a TIRF microscope, Figure 3B. By analyzing these images, the brightness of each tethered vesicle in each channel was quantified (see methods). The number of proteins attached to each vesicle was calculated by dividing its fluorescence intensity in the protein channel by the brightness of single molecules of the same fluorescent species. The distribution of vesicle diameters was measured using dynamic light scattering. This distribution was compared to the distribution of fluorescent intensities in the lipid fluorescence channel, providing an estimate of the diameter of each tethered vesicle (see methods). The average coverage of the vesicle surfaces by proteins, as a function of protein concentration in solution, was calculated by multiplying the average number of membrane-bound proteins per membrane area by the projected area per protein, 14.5 nm^2 [24], Figure 3C.

Using these data, the membrane area per polymer chain is simply the projected area of the polymer on the membrane surface, approximately 34 nm^2, divided by the total coverage of the membrane by proteins and polymers. Dividing the free energy calculated from equation 8 by the approximate area per polymer chain provides an estimate of the steric pressure experienced by the polymer chains. Therefore, the steric pressure is approximated as the change in free energy of the sensor per membrane area. Figure 3D plots this approximate steric pressure as a function of the coverage of the membrane surface by wtENTH. Here the pressure increases non-linearly as coverage increases, as expected from crowded particle theory [16].

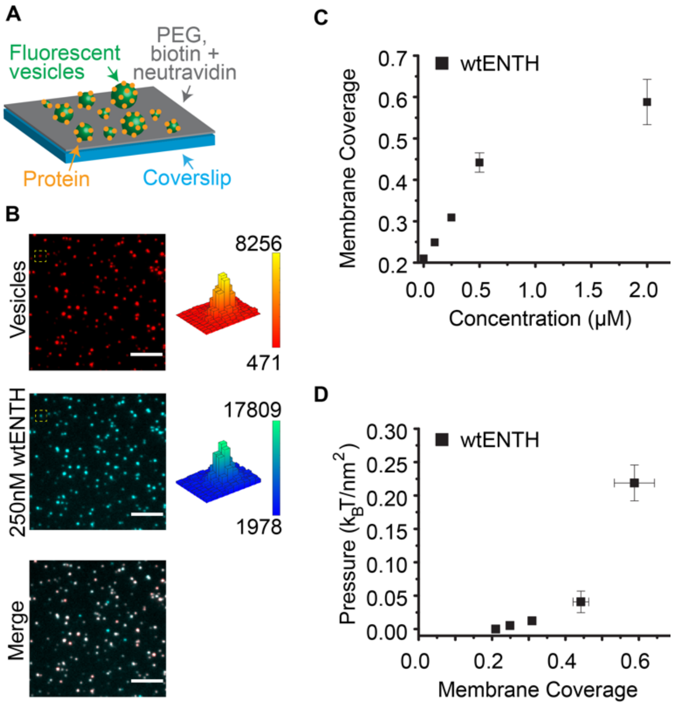

Figure 3 – Steric pressure is generated by crowded wtENTH proteins on membrane surfaces. The membrane composition was 67 mol% DOPC, 15 mol % DOPS, 5 mol% PtdIns(4,5)P2, 2 mol% DP-EG10-biotin, 1 mol% PEG 10K-DSPE, and 10 mol% Texas Red-DHPE for pressure measurement experiments. 1 mol% Texas Red-DHPE was used for membrane coverage measurements. Vesicles were extruded to a diameter of 100 nm. (A) Schematic of a tethered vesicle assay to measure membrane coverage of proteins on lipid vesicles. (B) Lipid, protein, and merged fluorescent images of SUVs and membrane-bound proteins. An example puncta is highlighted by a yellow box to show the fluorescence distribution in the lipid channel (red) and protein channel (cyan). Scale bar represents 5 μm. (C) Fractional coverage of the membrane surface by wtENTH domains as a function of wtENTH concentration in solution. (D) Approximate steric pressure generated by wtENTH at the membrane surface with increasing fractional membrane coverage. Vertical axis error bars in C were calculated as the standard error of the mean. Horizontal axis error bars in D were calculated as the standard error of the mean, while vertical axis error bars were calculated as the standard deviation of the mean.

.

ENTH generates steric pressure in good agreement with crowded particle theory, regardless of how it attaches to the membrane surface.

We next sought to determine the extent to which the specific chemistry used to attach ENTH to the membrane surface impacts these measurements. Specifically, we asked whether the amphipathic helix that wtENTH uses to bind to PI(4,5)P2 lipids is essential to generating steric pressure and remodeling membranes. To address this question we measured steric pressure generation and membrane remodeling by a version of the ENTH domain in which the amphipathic helix (AAs 1-16) is replaced by a 6 histidine tag, Figure 4A. The resulting his-ENTH protein binds to the surfaces of membrane vesicles containing 20 mol% Ni^{2+}-DGS-NTA lipids (1,2-dioleoyl-*sn*-glycero-3-[(N-(5-amino-1-carboxypentyl)iminodiacetic acid)succinyl]).

Using these vesicles, we examined the impact of increasing coverage of the membrane surface by his-ENTH proteins. As was the case for wtENTH, the coverage of the membrane surface by his-ENTH increases with increasing concentration of the protein in solution, Figure 4B. We next used the FRET sensor to examine steric pressure generation by his-ENTH. The resulting relationship between steric pressure and membrane coverage is plotted in Figure 4C, where it is compared to the data for wtENTH. Here his-ENTH and wtENTH follow similar trends, suggesting that generation of steric pressure at membrane surfaces is independent of the molecular interactions used to bring ENTH to the membrane surface.

The increase in steric pressure with increasing coverage of the membrane by ENTH has been previously predicted using the Carnahan Starling equation of state [16], a classic result from crowded particle theory, equation 9. Here p is steric pressure, η is the fractional coverage of the membrane surface by particles, and A_p is the area that an individual particle occupies.

$$p = \frac{4\eta}{A_p}\left(1 + 2\eta\frac{1-0.44\eta}{(1-\eta)^2}\right)k_B T \qquad (9)$$

Because the surfaces of the vesicles used in this study are covered by a mixture of PEG chains and ENTH domains, no single value of A_p exists, and equation 9 cannot be expected to agree precisely with the experimentally measured relationship between pressure and coverage. In Figure 4C we plot two curves, which represent the Carnahan Starling equation using the A_p value for the ENTH domain and the A_p value for the PEG chains, respectively. Comparing the data to these curves, we see that for low coverage values, where the polymer chains outnumber the protein domains, the data agree best with the curve that is based on the projected area of the PEG chains. In contrast, for high coverage values, where membrane-bound ENTH domains outnumber the polymer chains, the data are in better agreement with the curve that is based on the projected area of the ENTH domains. Notably, a similar relationship between steric pressure and protein coverage was measured using a 5 kilodalton PEG sensor (Supporting Figure 4), suggesting that changes in steric pressure arise primarily form membrane-bound proteins, rather than the sensor itself. Taken together, this comparison demonstrates that crowded particle theory provides a reasonable approximation of steric pressure on crowded membrane surfaces.

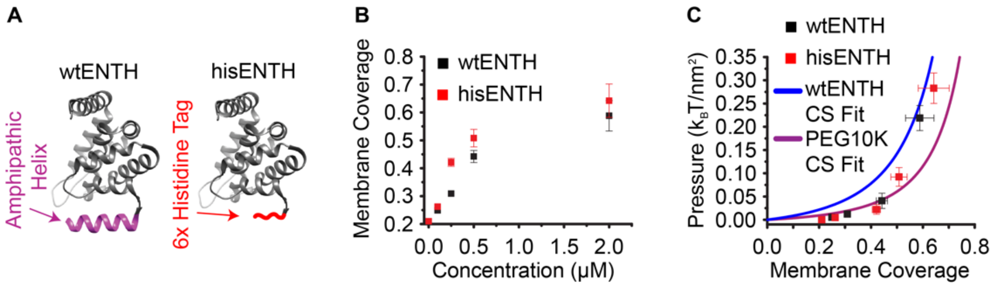

Figure 4 – Crowding of the membrane surface by hisENTH and wtENTH generates comparable levels of steric pressure. The membrane composition for hisENTH experiments was 67 mol% DOPC, 20 mol% DGS-NTA, 2 mol% DP-EG10-biotin, 1 mol%

PEG 10K-DSPE, and 10 mol% Texas Red-DHPE for pressure measurement experiments, extruded to a diameter of 100 nm. The membrane composition for wtENTH experiments was 67 mol% DOPC, 15 mol % DOPS, 5 mol% PtdIns(4,5)P2, 2 mol% DP-EG10-biotin, 1 mol% PEG 10K-DSPE, and 10 mol% Texas Red-DHPE for pressure measurement experiments, extruded to a diameter of 100 nm. 1 mol% Texas Red-DHPE was used for membrane coverage measurements. (A) Visual representation of the crystal structure of the ENTH domain. The hisENTH mutant has its amphipathic helix removed and replaced with a 6x histidine tag. (B) Fractional membrane coverage by hisENTH and wtENTH increase similarly with increasing concentration of protein in solution. (C) As hisENTH and wtENTH cover more of the membrane surface, we see a similar increase in steric pressure generated by both proteins. Data are compared to predictions of the Carnahan Starling equation of state (solid lines). Black markers in B-C represent an average from two independent experiments with 9-16 trials per experiment for a total of 18 to 32 total trials. Red markers in B-C represent an average from two independent experiments with 11-18 trials per experiment for a total of 22 to 36 total trials. Vertical axis error bars in B were calculated as the standard error of the mean. Horizontal axis error bars in C were calculated as the standard error of the mean, while vertical axis error bars were calculated as the standard deviation of the mean.

ENTH drives membrane remodeling by a mechanism that is largely independent of how it attaches to the membrane surface.

Finally, we examined the ability of wtENTH and his-ENTH to drive changes in vesicle diameter. Here we used a quantitative fluorescence approach to measure the size distribution of vesicles following protein exposure, a technique that we have reported previously [25]. Briefly, vesicles were incubated for 1 hour at room temperature with wtENTH or his-ENTH at concentrations ranging from 100 nM to 2 μM in solution. Following incubation, the distribution of vesicle sizes was determined using the quantitative fluorescence approach described above, producing the histograms shown in Figure 5A. These data were combined with the measurements of steric pressure (Figure 3D, 4C) and protein coverage (Figure 4B) for the same set of protein concentrations in order to obtain plots of vesicle size versus membrane coverage (Figure 5B) and vesicle size versus steric pressure (Figure 5C).

As the coverage of the membrane surface by ENTH proteins increased, the average vesicle diameter decreased to around 30 nm, Figure 5A. Importantly, we found that when wtENTH and his-ENTH were compared at equivalent membrane equivalent coverage, Figure 5B, or at equivalent steric pressure, Figure 5C, they generated very similar changes in vesicle diameter. These results demonstrate that ENTH's ability to remodel membranes is largely independent of the molecular interactions used to attach it to membrane surfaces. This result is significant because it is the first direct measurement of the ability of steric pressure to remodel membrane surfaces. These findings help to address the long-standing debate about the role of steric pressure in membrane remodeling [1, 6, 26].

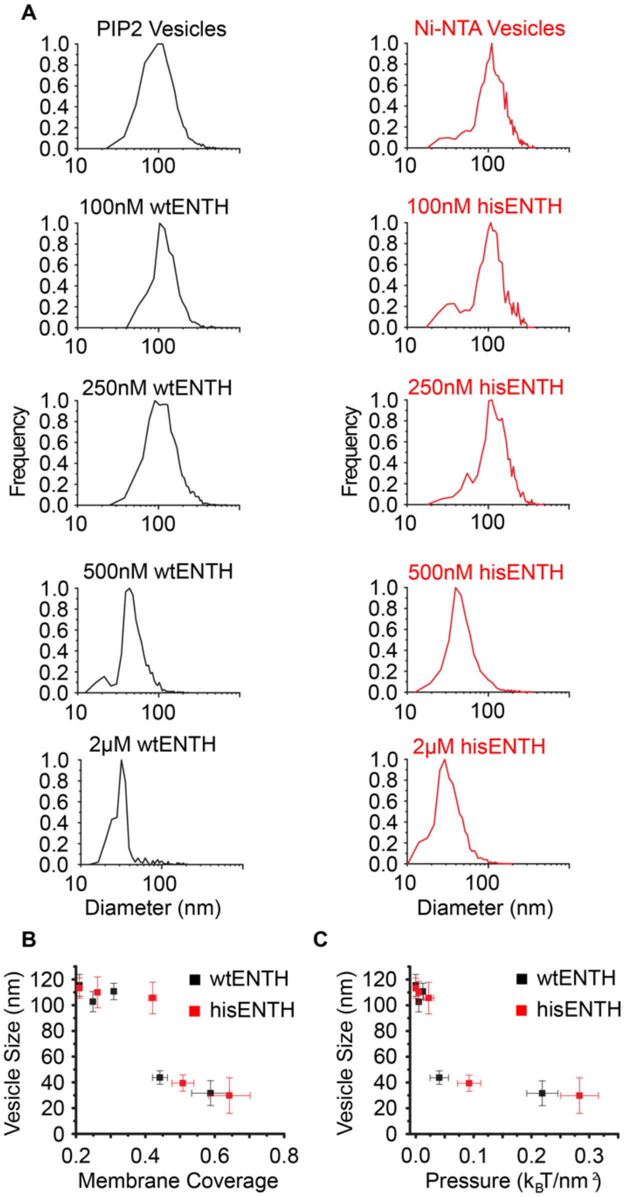

Figure 5 – Crowding of the membrane surface by wtENTH and hisENTH generates similar levels of membrane vesiculation. The membrane composition for hisENTH experiments was 67 mol% DOPC, 20 mol% DGS-NTA, 2 mol% DP-EG10-biotin, 1 mol% PEG 10K-DSPE, and 10 mol% Texas Red-DHPE for pressure measurement experiments, extruded to a diameter of 100 nm. The membrane composition for wtENTH experiments was 67 mol% DOPC, 15 mol % DOPS, 5 mol% PtdIns(4,5)P2, 2 mol% DP-EG10-biotin, 1 mol% PEG 10K-DSPE, and 10 mol% Texas Red-DHPE for pressure measurement experiments, extruded to a diameter of 100 nm. 1 mol% Texas Red-DHPE was used for membrane coverage measurements. (A) Distributions of vesicle diameter measured by tethered vesicle assay for wtENTH and hisENTH experiments. (B) Vesicle diameter of vesicles as a function of membrane coverage by wtENTH or hisENTH. (C) Vesicle diameter as a function of steric pressure generated by wtENTH or hisENTH. Black markers in B and C represent an average from two independent experiments with 9-16 trials per experiment for a total of 18 to 32 total trials. Red markers in B and C represent an average from two

independent experiments with 11-18 trials per experiment for a total of 22 to 36 total trials. Horizontal and vertical axis error bars in B were calculated as the standard error of the mean. Horizontal axis error bars in C were calculated as the standard deviation of the mean, while vertical axis error bars were calculated as the standard error of the mean.

Conclusions

Here we develop a FRET-based polymeric sensor of steric pressure on membrane surfaces. Using polymer theory to model the distribution of end-to-end distances for tethered polymers, we measured the impact of crowded conditions on polymer conformational entropy. Using this approach we estimated steric pressure at the membrane surface as a function of membrane coverage by crowding proteins. The resulting sensor accurately measured the increase in steric pressure with increasing coverage of the membrane surface by proteins, in good agreement with crowded particle theory. Importantly, the sensor was able to distinguish between steric pressure and other physiochemical effects at the membrane surface. In particular wtENTH, which bound to the membrane surface using hydrophobic interactions, and his-ENTH, which bound using electrostatic interactions, each generated the same trend of increasing steric pressure with increasing membrane coverage, Figure 4C. Further, we correlated steric pressure generation with the breakup of larger membrane vesicles into smaller ones, Figure 5C, revealing nearly identical trends for wtENTH and his-ENTH. These results are the first to directly demonstrate that steric pressure, rather than the mechanism of protein attachment to the membrane surface, is the key driver of membrane vesiculation by ENTH. More broadly, our experiments, when combined with polymer theory, provide a universal way to assess crowding-induced pressure on membranes. Notably, the method could be used to obtain steric pressure regardless of the nature of interaction between the crowding particles and the membrane.

By developing the first sensor for steric pressure at membrane surfaces, this work expands our ability to study steric effects in diverse membrane environments. Prior to the development of this sensor, steric pressure was inferred from crowded particle theory. However, this strategy requires precise knowledge of the number and size of all membrane-bound proteins, making it inappropriate for analyzing complex environments. Here we have used crowded particle theory to validate our novel sensor in a controlled membrane environment. Building on this foundation, our sensor can now be used to probe the growing list of biological contexts in which steric pressure is thought to impact membrane biology. These include budding of lipid droplets [27], protrusions of the plasma membrane driven by steric pressure within the glycocalyx [9], budding of endocytic vesicles [28], and changes in membrane phase separation [17] and mobility [18]. In these and many other contexts, measuring the mechanical forces that arise from the inherently crowded nature of biological membranes is important for understanding the biophysical mechanisms that control membrane shape and organization.

Materials and Methods

Lipid vesicle preparation for FRET

Small unilamellar vesicles (SUVs) were prepared, which incorporated 1 mol% of lipids with PEG chains of various molecular weight (2kDa, 3.4kDa, 5kDa, and 10kDa MW), covalently attached to 1,2-distearoyl-*sn*-glycero-3-phosphoethanolamine (DSPE) to form DSPE-PEG-NH2, (1,2-Distearoyl-sn-Glycero-3-Phosphoethanolamine (DSPE)-polyethylene glycol-amine) These DSPE-PEG-NH2 lipids were purchased from Nanosoft Polymers and used without additional purification. We labeled the amine groups at the ends of the PEG chains with donor fluorophores, as described below. Texas Red covalently attached to 1,2-Dihexadecanoyl-*sn*-Glycero-3-Phosphoethanolamine (DHPE) served as the acceptor fluorophore in the FRET system, and was included in the lipid composition at 2.5 to 10 mol%, as described in the results section. 20 mol% of 1,2-dioleoyl-sn glycero-3-[(N-(5-amino-1-carboxypentyl)iminodiacetic acid)succinyl] nickel salt (Ni^{2+}-DGS-NTA) was used to bind his-ENTH proteins in all experiments. 5 mol% PtdIns(4,5)P2 and 15 mol% 1,2-dioleoyl-sn-glycero-3-phospho-L-serine (DOPS) were used to bind wtENTH in all experiments. The remainder of each vesicle composition consisted of 1,2-dioleoyl-sn-glycero-3-phosphocholine (DOPC). The lipids, dissolved in the appropriate solvent (chloroform or chloroform/methanol for PI(4.5)P2 lipids) were mixed in a clean glass test tube. The solvent was evaporated, and the lipid film was further dried under vacuum overnight. The dried lipid film was hydrated in 20 mM sodium bicarbonate, 150 mM KCl, pH 8.2 at room temperature for 15 minutes. The lipid mixture was then extruded through a filter with 100 nm pores. The extruded vesicles were then incubated with the donor dye (100 µM of NHS-ester functionalized ATTO 488) for 2 hours at room temperature. We then successively washed the excess dye out from the mixture using 100K Amicon spin filter units. In order to minimize background levels of free dye in solution, the solution surrounding the vesicle was effectively diluted by 10^{14} fold during the washing step, where the vesicles were finally left in the experimental buffer consisting of 25 mM Hepes, 150 mM NaCl, pH 7.35.

Quantitative FRET Measurements by TCSPC

Lipid vesicles were prepared as previously described in the “Lipid vesicle preparation for FRET” section. Coverslips with 1.5 thickness (13-16 µm) were cleaned by a heated acid, base, and hydrogen peroxide washing technique. To passivate the surface of the coverslip before imaging, we created a supported lipid bilayer in small silicone wells on the coverslip. This coating prevented significant lipid or protein binding to the coverslip. We then added the lipid vesicle mixture to the wells and proceeded to collect fluorescence lifetime data. A homebuilt confocal microscope was used to acquire all lifetime data. Vesicles diffused freely in solution, passing through the focal volume throughout the 150-200 second integration time of the measurements. A 486 nm picosecond pulsed diode laser at a repetition rate of 50 MHz was used to excite the donor fluorophore (ATTO 488). The laser beam was focused 5 µm above the surface of the glass coverslip using a piezo stage (Mad City Labs). Sample fluorescence was collected by a 100x magnification 1.45 NA microscope objective, focused through a pinhole onto a GaAsP photomultiplier tube (Hamamatsu). Sample fluorescence was passed through a 511 nm bandpass emission filter with a 10 nm bandwidth before arriving at the photomultiplier tube. The photomultiplier tube output pulses were amplified and sent to a computer card for time-correlated single-photon counting (Becker and Hickl). Donor fluorescence decay curves were collected for 100-300 seconds, and 9-30 decay curves were collected across at least two independent samples per data point.

Protein Expression and Purification

The wild-type ENTH domain of rat epsin1 (wtENTH) was expressed as an N-terminal glutathione-S-transferase (GST) fusion proteins in E. coli BL21 cells following induction with 0.5 mM IPTG for 3 hours at 37 °C. Bacteria were lysed using 0.1% Tween 20 and probe sonication for 5 minutes. Protein was purified from bacterial extracts by incubating with glutathione agarose beads in 25 mM HEPES, 150mM NaCl, 5 mM β-mercaptoethanol, pH 7.35 for 1 hour at 4°C. After washing (10x column volumes), protein was cleaved from the beads overnight rocking at 15 °C with thrombin. Excess thrombin was removed by incubation with p-aminobenzamidine-agarose for 30 minutes at 4°C.

A mutant of the wild-type ENTH domain lacking the N-terminal helix (first 16 amino acids) was expressed as an N-terminal hexa-histidine fusion protein in BL21 cells following overnight induction at 18 °C with 1 mM IPTG. Bacteria were lysed using 0.1% Tween 20 and probe sonication for 5 minutes. Protein was purified from bacterial extracts by incubating with Ni-NTA agarose beads in 25 mM HEPES, 150 mM NaCl, 5 mM β-mercaptoethanol, pH 7.35 buffer. After extensive washing of the beads (10x column volumes), protein was eluted from Ni-NTA resin by gradually increasing to a final buffer concentration of 200 mM imidazole. Eluted protein was concentrated in spin-filters by centrifugation and dialyzed against 4L of 25 mM HEPES, 150 mM NaCl, 5 mM β-mercaptoethanol, pH 7.35 at 4 °C overnight.

Measuring Membrane Coverage by wtENTH and hisENTH

We used a fluorescence brightness-based approach, which we have previously reported [11], to obtain a measure of membrane coverage by wtENTH and his-ENTH. Vesicles for experiments with wtENTH were composed of 76 mol% DOPC, 15 mol % DOPS, 5 mol% PtdIns(4,5)P2, 2 mol% DP-EG10-biotin, 1 mol% PEG 10K-DSPE, and 1 mol% Texas Red-DHPE. DOPS and PtdIns(4,5)P2 were replaced by 20 mol % DGS-NTA for his-ENTH experiments. Lipid vesicles were prepared as described above. Imaging wells were made by placing silicone gaskets onto ultraclean coverslips. Wells were coated for 20 minutes with biotinylated PLL-PEG. The biotinylated PLL-PEG was made according to a previously published protocol [29]. After incubation, the well was washed repeatedly with a buffer containing 25 mM Hepes, 150 mM NaCl, 5mM TCEP pH 7.35. Neutravidin was added to the well at a final concentration of 0.2 mg/mL, incubated for 10 min, and washed out with HEPES buffer. Vesicles were diluted to 2 μM and incubated with increasing concentrations of Alexa 647 labeled proteins (his-ENTH or wtENTH) in microcentrifuge tubes for 1 hour. After incubation of protein with the vesicles, the mixture was pipetted onto the imaging well prepared with PLL-PEG neutravidin. The biotinylated lipid tethered the protein-coated vesicles onto the neutravidin coated surface. The tethered vesicles were then imaged on a home built total internal reflection fluorescence (TIRF) microscope. A continuous wave 532 nm diode laser was used to excite Texas Red-DHPE, and a 640 nm diode laser was used to excite Alexa 647. The TIRF angle was calibrated such that 100 nm vesicles were homogenously illuminated. At least 10 images were taken for each protein concentration. All images were cropped to the center 171x171 pixels of the 512x512 pixel field of view. Fluorescence amplitudes of diffraction-limited puncta were obtained using the cmeAnalysis particle detection software [30]. This program detected individual vesicles by fitting two-dimensional Gaussian profiles to each puncta in the lipid fluorescence channel. We then used the centroids of the fluorescent puncta in the lipid channel to define the search region for fluorescent puncta in the protein channel. The dimension of the search region was three times the standard deviation of the Gaussian fit to the point spread function of our microscope. Using these detected fluorescent intensities, we estimated vesicle diameter from lipid fluorescence values by computing a scaling factor, which centered the median of the vesicle brightness distribution, prior to adding protein, to the intensity-weighted average vesicle diameter obtained from dynamic light scattering. We estimated the number of bound proteins on each vesicle by comparing brightness values in the protein channel to the brightness of a single molecule of Alexa 647 labeled wtENTH, which was measured using the same microscope settings. Membrane coverage was then estimated by dividing the total area occupied by the bound proteins by the approximate surface area of the vesicle, assuming one ENTH protein occupies an area of approximately 14.5 nm^2 on the membrane surface.

Measuring the coverage of the vesicle surface by the PEG-based sensor

In order to quantify the coverage of PEG 10K on the surface of our vesicles, we used a single molecule calibration approach to count the number of PEG chains on individual vesicles. First, in order to ensure we labeled all of the available PEG chains on the surface of the vesicles, we tested different labeling conditions. We increased the amount of dye in solution with the vesicles until we observed a plateau of the amount of dye molecules conjugated to the vesicles. Lipid vesicles with a composition of 97 mol% DOPC, 2 mol% DP-EG10-biotin, and 1 mol% PEG 10K-DSPE-NH2 were extruded to 100 nm in 20 mM Sodium bicarbonate, 150 mM potassium chloride pH 8.2 buffer. Varying molar excess of NHS-Ester ATTO 488 dye (0.5x to 20x) was added in solution with the vesicles at room temperature for 2 hours. After labeling, we washed the excess dye out from the vesicle mixture by 100K Amicon spin filter units. In order to reach acceptable background levels of free dye in solution, we empirically arrived at a washing method of 7x washes of a 10x dilution with buffer in one spin filter unit, transferring the lipid mixture to a new spin filter unit and washing another 7 times. Absorbance measurements by UV-VIS spectroscopy were then taken on the washed vesicles (FIG S3 A). Two sets of experiments were performed with three trials per labeling condition (FIG S3 B). All labeling of DSPE-PEG-NH2 in the main text was performed at 20x molar excess of dye to PEG. Coverage measurements were then performed on another set of vesicles with a small percentage of Texas Red DHPE (0.05%) to visualize the vesicles by fluorescence microscopy. Two sets of experiments with 7-8 trials per experiment were performed by spinning disk confocal microscopy. Image acquisition, processing, and single molecule calibration were performed as described in the “Measuring Membrane Coverage by wtENTH and hisENTH” methods section in the main text. From this analysis we arrive at a quantitative number of PEG chains per vesicle. Coverage of PEG10K on the vesicles was calculated as follows:

$$C = \frac{P_R A_P}{4\pi\left(R + r_p\right)^2} \quad \text{Equation S1}$$

Where C is coverage, P_R is number of PEG chains on vesicles of radius R, A_P is the area PEG 10K occupies on the membrane (34 nm^2), and r_p is the radius of gyration of PEG 10K (3.3 nm). Using equation S1 we calculated the coverage of PEG 10K on all of the vesicles imaged. We took the median of the data shown in Supporting Figures S3C and arrived at a coverage of approximately 21%. This value was added to the protein coverage in all the main text figures where coverage was measured.

Measuring Membrane Fission by wtENTH and hisENTH

To measure membrane fission, we used the experimental methods described in the “Measuring Membrane Coverage by wtENTH and hisENTH” section to measure vesicle size over a range of membrane coverages. Briefly, vesicles for experiments with wtENTH were composed of 76 mol% DOPC, 15 mol % DOPS, 5 mol% PtdIns(4,5)P2, 2 mol% DP-EG10-biotin, 1 mol% PEG 10K-DSPE, and 1 mol% Texas Red-DHPE. DOPS and PtdIns(4,5)P2 were replaced by 20 mol % DGS-NTA for his-ENTH experiments. Lipid vesicles were prepared as described in the “Lipid vesicle preparation for FRET” methods section. WtENTH or hisENTH proteins at varying concentrations (100 nM to 2 μM) were incubated with vesicles for 1 hour at room temperature. The protein-vesicle solution was then tethered to the biotinylated PLL-PEG functionalized coverslip for 10 minutes. Image acquisition and analysis was performed as described above. Notably, we estimated vesicle diameter from lipid fluorescence values by computing a scaling factor, which centered the median of the vesicle brightness distribution, prior to adding protein, to the intensity-weighted average vesicle diameter obtained from dynamic light scattering (DLS). This DLS measurement was performed for every set of vesicles created the day of the experiment. After addition of protein to the sample, the fluorescence intensity of each tethered vesicle puncta in the lipid channel decreased according to how much fission occurred and how small the vesicles became. This change in vesicle size over a range of membrane coverages by wtENTH or hisENTH is shown in Figure 5B and 5C.

Supporting Information

The electronic supporting information includes additional supporting data in the form of Supporting Figures 1-4, and Supporting Table 1.

Acknowledgements

This research was supported by the National Science Foundation through a Modulus grant: BIO-1934509 to J.C.S., and by CHE 19-00093 to D.T. This work was also supported by the Welch Foundation through grants F-2047 to J.C.S and F-0019 to D.T., and by the Collie-Welch chair (D.T.), and by a grant from the National Institutes of Health (R01GM120549) to J.C.S.

References

1. Stachowiak, J. C.; Brodsky, F. M.; Miller, E. A., A cost-benefit analysis of the physical mechanisms of membrane curvature. *Nature Cell Biology* **2013,** *15* (9), 1019-27.
2. Praefcke, G. J.; McMahon, H. T., The dynamin superfamily: universal membrane tubulation and fission molecules? *Nature reviews. Molecular cell biology* **2004,** *5* (2), 133-47.
3. Jiang, Z.; de Messieres, M.; Lee, J. C., Membrane remodeling by alpha-synuclein and effects on amyloid formation. *Journal of the American Chemical Society* **2013,** *135* (43), 15970-3.
4. Ford, M.; Mills, I.; Peter, B.; Vallis, Y.; Praefcke, G.; Evans, P.; McMahon, H., Curvature of clathrin-coated pits driven by epsin. *Nature* **2002,** *419* (6905), 361-366.
5. Stachowiak, J. C.; Hayden, C. C.; Sasaki, D. Y., Steric confinement of proteins on lipid membranes can drive curvature and tubulation. *Proc Natl Acad Sci U S A* **2010,** *107* (17), 7781-6.
6. Stachowiak, J.; Schmid, E.; Ryan, C.; Ann, H.; Sasaki, D.; Sherman, M.; Geissler, P.; Fletcher, D.; Hayden, C., Membrane bending by protein-protein crowding. *Nature Cell Biology* **2012,** *14* (9), 944-49.
7. Shi, Z.; Baumgart, T., Membrane tension and peripheral protein density mediate membrane shape transitions. *Nature Communications* **2015,** *6*, 5974.
8. Zhu, C.; Das, S. L.; Baumgart, T., Nonlinear sorting, curvature generation, and crowding of endophilin N-BAR on tubular membranes. *Biophys. J.* **2012,** *102* (8), 1837-45.
9. Shurer, C. R.; Kuo, J. C.; Roberts, L. M.; Gandhi, J. G.; Colville, M. J.; Enoki, T. A.; Pan, H.; Su, J.; Noble, J. M.; Hollander, M. J.; O'Donnell, J. P.; Yin, R.; Pedram, K.; Mockl, L.; Kourkoutis, L. F.; Moerner, W. E.; Bertozzi, C. R.; Feigenson, G. W.; Reesink, H. L.; Paszek, M. J., Physical Principles of Membrane Shape Regulation by the Glycocalyx. *Cell* **2019,** *177* (7), 1757-1770 e21.
10. Busch, D. J.; Houser, J. R.; Hayden, C. C.; Sherman, M. B.; Lafer, E. M.; Stachowiak, J. C., Intrinsically disordered proteins drive membrane curvature. *Nature Communications* **2015,** *6*, 7875.
11. Snead, W. T.; Hayden, C. C.; Gadok, A. K.; Zhao, C.; Lafer, E. M.; Rangamani, P.; Stachowiak, J. C., Membrane fission by protein crowding. *P Natl Acad Sci USA* **2017,** *114* (16), E3258-E3267.
12. Derganc, J.; Copic, A., Membrane bending by protein crowding is affected by protein lateral confinement. *Biochim Biophys Acta* **2016,** *1858* (6), 1152-9.
13. Soranno, A.; Koenig, I.; Borgia, M. B.; Hofmann, H.; Zosel, F.; Nettels, D.; Schuler, B., Single-molecule spectroscopy reveals polymer effects of disordered proteins in crowded environments. *P Natl Acad Sci USA* **2014,** *111* (13), 4874-9.
14. DiMarzio, E. A., Proper accounting of conformations of a polymer near a surface. *The Journal of Chemical Physics* **1965,** *42* (6), 2101-2106.
15. Dimarzio, E. A.; McCrackin, F. L., One-dimensional model of polymer adsorption. *The Journal of Chemical Physics* **1965,** *43* (2), 539-547.

16. Carnahan, N. F.; Starling, K. E., Equation of State for Nonattracting Rigid Spheres. *Journal of Chemical Physics* **1969,** *51* (2), 635-&.

17. Scheve, C. S.; Gonzales, P. A.; Momin, N.; Stachowiak, J. C., Steric pressure between membrane-bound proteins opposes lipid phase separation. *Journal of the American Chemical Society* **2013,** *135* (4), 1185-8.

18. Houser, J. R.; Busch, D. J.; Bell, D. R.; Li, B.; Ren, P.; Stachowiak, J. C., The impact of physiological crowding on the diffusivity of membrane bound proteins. *Soft Matter* **2016,** *12* (7), 2127-34.

19. Hughes, L. D.; Rawle, R. J.; Boxer, S. G., Choose your label wisely: water-soluble fluorophores often interact with lipid bilayers. *PLoS One* **2014,** *9* (2), e87649.

20. Flory, P. J., *Statistical mechanics of chain molecules*. Repr. ed.; Hanser Publishers ;Distributed in the U.S.A. by Oxford University Press: Munich ; New York, New York, 1989; p xxv, 432 p.

21. Kienberger, F.; Pastushenko, V. P.; Kada, G.; Gruber, H. J.; Riener, C.; Schindler, H.; Hinterdorfer, P., Static and Dynamical Properties of Single Poly(Ethylene Glycol) Molecules Investigated by Force Spectroscopy. *Single Molecules* **2000,** *1*, 123-128.

22. Carignano, M. A.; Szleifer, I., On the Structure and Pressure of Tethered Polymer Layers in Good Solvent. *Macromolecules* **1995,** *28*, 3197-3204.

23. Takamori, S.; Holt, M.; Stenius, K.; Lemke, E. A.; Gronborg, M.; Riedel, D.; Urlaub, H.; Schenck, S.; Brugger, B.; Ringler, P.; Muller, S. A.; Rammner, B.; Grater, F.; Hub, J. S.; De Groot, B. L.; Mieskes, G.; Moriyama, Y.; Klingauf, J.; Grubmuller, H.; Heuser, J.; Wieland, F.; Jahn, R., Molecular anatomy of a trafficking organelle. *Cell* **2006,** *127* (4), 831-46.

24. Hyman, J.; Chen, H.; Di Fiore, P. P.; De Camilli, P.; Brunger, A. T., Epsin 1 undergoes nucleocytosolic shuttling and its Eps15 interactor NH2-terminal homology (ENTH) domain, structurally similar to Armadillo and HEAT repeats, interacts with the transcription factor promyelocytic leukemia Zn2+ finger protein (PLZF). *Journal of Cell Biology* **2000,** *149* (3), 537-546.

25. Snead, W. T.; Stachowiak, J. C., A Tethered Vesicle Assay for High-Throughput Quantification of Membrane Fission. *Method Enzymol* **2018,** *611*, 559-582.

26. Kozlov, M. M.; Campelo, F.; Liska, N.; Chernomordik, L. V.; Marrink, S. J.; McMahon, H. T., Mechanisms shaping cell membranes. *Current Opinion in Cell Biology* **2014,** *29*, 53-60.

27. Kory, N.; Thiam, A.; Farese, R.; Walther, T., Protein Crowding Is a Determinant of Lipid Droplet Protein Composition. *Dev Cell* **2015,** *34* (3), 351-363.

28. Snead, W. T.; Stachowiak, J. C., Structure Versus Stochasticity-The Role of Molecular Crowding and Intrinsic Disorder in Membrane Fission. *J Mol Biol* **2018,** *430* (16), 2293-2308.

29. Ruiz-Taylor, L.; Martin, T.; Zaugg, F.; Witte, K.; Indermuhle, P.; Nock, S.; Wagner, P., Monolayers of derivatized poly (L-lysine)-grafted poly (ethylene glycol) on metal oxides as a class of biomolecular interfaces. *Proceedings of the National Academy of Sciences* **2001,** *98* (3), 852-857.

30. Aguet, F.; Antonescu, C. N.; Mettlen, M.; Schmid, S. L.; Danuser, G., Advances in analysis of low signal-to-noise images link dynamin and AP2 to the functions of an endocytic checkpoint. *Dev Cell* **2013,** *26* (3), 279-291.

Table of Contents Graphic